Research Article | Vol. 9, No. 2 | 1 Feb 2018 | BIOMEDICAL OPTICS EXPRESS 453
Biomedical Optics EXPRESS

Spectrum- and time-resolved endogenous multiphoton signals reveal quantitative differentiation of premalignant and malignant gastric mucosa

XI LI,[1,5] HUI LI,[2,5] XINGZHEN HE,[3] TINGAI CHEN,[2] XIANYUAN XIA,[2] CHUNXIA YANG,[4] AND WEI ZHENG[2,*]

[1]*Department of Gastroenterology, Peking University Shenzhen Hospital, Shen Zhen 518036, China*
[2]*Research Laboratory for Biomedical Optics and Molecular Imaging, Shenzhen Institutes of Advanced Technology, Chinese Academy of Sciences, Shenzhen 518055, China*
[3]*Department of Gastroenterology, Zhejiang Hospital, Hangzhou 310007, China*
[4]*Department of Pathology, Jinchang First People's Hospital, Jinchang 737109, China*
[5]*Authors contributed equally to this work*
[*]*zhengwei@siat.ac.cn*

Abstract: Early identification of premalignant and malignant gastric mucosa is crucial to decrease the incidence and mortality of stomach cancer. Spectrum- and time-resolved multiphoton microscopy are capable of providing not only structural but also biochemical information at the subcellular level. Based on this multidimensional imaging technique, we performed a systematic investigation on fresh human tissue specimens at the typical stages of gastric carcinogenesis, including normal, chronic gastritis with erosion, chronic gastritis with intestinal metaplasia, and intestinal-type adenocarcinoma. The results demonstrate that this technique is available to characterize the three-dimensional subcellular morphological and biochemical properties of gastric mucosa and further provide quantitative indicators of different gastric disorders, by using endogenous contrast. With advances in multiphoton endoscopy, it has the potential to allow noninvasive, label-free, real-time histological and functional diagnosis of premalignant and malignant lesions of stomach in the future.

OCIS codes: (180.4315) Nonlinear microscopy; (300.6500) Spectroscopy, time-resolved; (170.2680) Gastrointestinal; (170.3880) Medical and biological imaging.

References and links

1. L. A. Torre, F. Bray, R. L. Siegel, J. Ferlay, J. Lortet-Tieulent, and A. Jemal, "Global cancer statistics, 2012," CA Cancer J. Clin. **65**(2), 87–108 (2015).
2. B. W. Stewart and C. P. Wild, *World cancer report 2014* (WHO Press, 2015).
3. V. Kumar, M. E. A. Abbas, N. Fausto, A. Abbas, J. Aster, V. Kumar, N. Fausto, R. Cotran, T. Agurs-Collins, S. Robbins, and R. Contran, *Pathologic Basis of Disease* (Saunders Elsevier, 2010).
4. P. Correa, "Human gastric carcinogenesis: a multistep and multifactorial process-First American Cancer Society Award Lecture on Cancer Epidemiology and Prevention," Cancer Res. **52**(24), 6735–6740 (1992).
5. K. Wirths and H. Neuhaus, "Endomicroscopy of gastritis and gastric cancer," in *Atlas of Endomicroscopy* (Springer Berlin Heidelberg, 2008), pp. 60–66.
6. H. Bao, A. Boussioutas, J. Reynolds, S. Russell, and M. Gu, "Imaging of goblet cells as a marker for intestinal metaplasia of the stomach by one-photon and two-photon fluorescence endomicroscopy," J. Biomed. Opt. **14**(6), 064031 (2009).
7. J. Yan, G. Chen, J. Chen, N. Liu, S. Zhuo, H. Yu, and M. Ying, "A pilot study of using multiphoton microscopy to diagnose gastric cancer," Surg. Endosc. **25**(5), 1425–1430 (2011).
8. Z. Wang, W. Zheng, J. Lin, and Z. Huang, "Simultaneous quadruple-modal nonlinear optical imaging for gastric diseases diagnosis and characterization," Proc. SPIE **9329**, 93291P (2015).
9. S. Fujiwara, K. Yao, T. Nagahama, K. Uchita, T. Kanemitsu, K. Tsurumi, N. Takatsu, T. Hisabe, H. Tanabe, A. Iwashita, and T. Matsui, "Can we accurately diagnose minute gastric cancers (≤5 mm)? Chromoendoscopy (CE) vs magnifying endoscopy with narrow band imaging (M-NBI)," Gastric Cancer **18**(3), 590–596 (2015).
10. H. Kikuchi, K. Kamiya, Y. Hiramatsu, S. Miyazaki, M. Yamamoto, M. Ohta, S. Baba, and H. Konno, "Laparoscopic narrow-band imaging for the diagnosis of peritoneal metastasis in gastric cancer," Ann. Surg. Oncol. **21**(12), 3954–3962 (2014).

#308583 https://doi.org/10.1364/BOE.9.000453
Journal © 2018 Received 6 Oct 2017; revised 25 Dec 2017; accepted 30 Dec 2017; published 8 Jan 2018

Biomedical Optics EXPRESS

11. M. Kobayashi, H. Tajiri, E. Seike, M. Shitaya, S. Tounou, M. Mine, and K. Oba, "Detection of early gastric cancer by a real-time autofluorescence imaging system," Cancer Lett. **165**(2), 155–159 (2001).
12. K. Yao, G. K. Anagnostopoulos, and K. Ragunath, "Magnifying endoscopy for diagnosing and delineating early gastric cancer," Endoscopy **41**(5), 462–467 (2009).
13. J. Shi, N. Jin, Y. Li, S. Wei, and L. Xu, "Clinical study of autofluorescence imaging combined with narrow band imaging in diagnosing early gastric cancer and precancerous lesions," J. BUON **20**(5), 1215–1222 (2015).
14. K. Yao, H. Doyama, T. Gotoda, H. Ishikawa, T. Nagahama, C. Yokoi, I. Oda, H. Machida, K. Uchita, and M. Tabuchi, "Diagnostic performance and limitations of magnifying narrow-band imaging in screening endoscopy of early gastric cancer: a prospective multicenter feasibility study," Gastric Cancer **17**(4), 669–679 (2014).
15. X. M. Meng, Y. Zhou, T. Dang, X. Y. Tian, and J. Kong, "Magnifying chromoendoscopy combined with immunohistochemical staining for early diagnosis of gastric cancer," World J. Gastroenterol. **19**(3), 404–410 (2013).
16. P. E. Paull, B. J. Hyatt, W. Wassef, and A. H. Fischer, "Confocal laser endomicroscopy: a primer for pathologists," Arch. Pathol. Lab. Med. **135**(10), 1343–1348 (2011).
17. M. Goetz, "Confocal laser endomicroscopy: applications in clinical and translational science—a comprehensive review," ISRN Pathol. **2012**, 387145 (2012).
18. F. Helmchen and W. Denk, "Deep tissue two-photon microscopy," Nat. Methods **2**(12), 932–940 (2005).
19. W. R. Zipfel, R. M. Williams, R. Christie, A. Y. Nikitin, B. T. Hyman, and W. W. Webb, "Live tissue intrinsic emission microscopy using multiphoton-excited native fluorescence and second harmonic generation," Proc. Natl. Acad. Sci. U.S.A. **100**(12), 7075–7080 (2003).
20. H. Li, Q. Cui, Z. Zhang, L. Fu, and Q. Luo, "Nonlinear optical microscopy for immunoimaging: a custom optimized system of high-speed, large-area, multicolor imaging," Quant. Imaging Med. Surg. **5**(1), 30–39 (2015).
21. R. Cicchi, A. Sturiale, G. Nesi, D. Kapsokalyvas, G. Alemanno, F. Tonelli, and F. S. Pavone, "Multiphoton morpho-functional imaging of healthy colon mucosa, adenomatous polyp and adenocarcinoma," Biomed. Opt. Express **4**(7), 1204–1213 (2013).
22. J. N. Rogart, J. Nagata, C. S. Loeser, R. D. Roorda, H. Aslanian, M. E. Robert, W. R. Zipfel, and M. H. Nathanson, "Multiphoton imaging can be used for microscopic examination of intact human gastrointestinal mucosa ex vivo," Clin. Gastroenterol. Hepatol. **6**(1), 95–101 (2008).
23. L. E. Grosberg, A. J. Radosevich, S. Asfaha, T. C. Wang, and E. M. Hillman, "Spectral characterization and unmixing of intrinsic contrast in intact normal and diseased gastric tissues using hyperspectral two-photon microscopy," PLoS One **6**(5), e19925 (2011).
24. L. Marcu, "Fluorescence lifetime techniques in medical applications," Ann. Biomed. Eng. **40**(2), 304–331 (2012).
25. D. Chorvat, Jr. and A. Chorvatova, "Multi-wavelength fluorescence lifetime spectroscopy: a new approach to the study of endogenous fluorescence in living cells and tissues," Laser Phys. Lett. **6**(3), 175–193 (2009).
26. W. Becker and A. Bergmann, "Lifetime-resolved imaging in nonlinear microscopy," in *Handbook of Biomedical Nonlinear Optical Microscopy*, B. R. Masters and P. T. C. So, eds. (Oxford University Press, 2008), pp. 499–556.
27. E. Stuntz, Y. Gong, D. Sood, V. Liaudanskaya, D. Pouli, K. P. Quinn, C. Alonzo, Z. Liu, D. L. Kaplan, and I. Georgakoudi, "Endogenous two-photon excited fluorescence imaging characterizes neuron and astrocyte metabolic responses to manganese toxicity," Sci. Rep. **7**(1), 1041 (2017).
28. S. K. Teh, W. Zheng, S. Li, D. Li, Y. Zeng, Y. Yang, and J. Y. Qu, "Multimodal nonlinear optical microscopy improves the accuracy of early diagnosis of squamous intraepithelial neoplasia," J. Biomed. Opt. **18**(3), 036001 (2013).
29. J. Leppert, J. Krajewski, S. R. Kantelhardt, S. Schlaffer, N. Petkus, E. Reusche, G. Hüttmann, and A. Giese, "Multiphoton excitation of autofluorescence for microscopy of glioma tissue," Neurosurgery **58**(4), 759–767 (2006).
30. Y. Wu, W. Zheng, and J. Y. Qu, "Sensing cell metabolism by time-resolved autofluorescence," Opt. Lett. **31**(21), 3122–3124 (2006).
31. K. König, A. Ehlers, I. Riemann, S. Schenkl, R. Bückle, and M. Kaatz, "Clinical two-photon microendoscopy," Microsc. Res. Tech. **70**(5), 398–402 (2007).
32. D. M. Huland, D. G. Ouzounov, D. R. Rivera, C. M. Brown, and C. Xu, "Intravital multiphoton endoscopy," in *Advances in Intravital Microscopy: From Basic to Clinical Research*, R. Weigert, ed. (Springer Netherlands, 2014), pp. 305–370.
33. S. Zhang, "Digestive system," in *An Atlas of Histology*, S. Zhang, ed. (Springer New York, 1999), pp. 187–251.
34. J. J. Engelhardt, B. Boldajipour, P. Beemiller, P. Pandurangi, C. Sorensen, Z. Werb, M. Egeblad, and M. F. Krummel, "Marginating dendritic cells of the tumor microenvironment cross-present tumor antigens and stably engage tumor-specific T cells," Cancer Cell **21**(3), 402–417 (2012).
35. D. Li, W. Zheng, and J. Y. Qu, "Time-resolved spectroscopic imaging reveals the fundamentals of cellular NADH fluorescence," Opt. Lett. **33**(20), 2365–2367 (2008).
36. W. Hu, G. Zhao, C. Wang, J. Zhang, and L. Fu, "Nonlinear optical microscopy for histology of fresh normal and cancerous pancreatic tissues," PLoS One **7**(5), e37962 (2012).
37. R. Datta, C. Heylman, S. C. George, and E. Gratton, "Label-free imaging of metabolism and oxidative stress in human induced pluripotent stem cell-derived cardiomyocytes," Biomed. Opt. Express **7**(5), 1690–1701 (2016).

Biomedical Optics EXPRESS

38. J.-M. Salmon, E. Kohen, P. Viallet, J. G. Hirschberg, A. W. Wouters, C. Kohen, and B. Thorell, "Microspectrofluorometric approach to the study of free/bound NAD(P)H ratio as metabolic indicator in various cell types," Photochem. Photobiol. **36**(5), 585–593 (1982).
39. A. Pradhan, P. Pal, G. Durocher, L. Villeneuve, A. Balassy, F. Babai, L. Gaboury, and L. Blanchard, "Steady state and time-resolved fluorescence properties of metastatic and non-metastatic malignant cells from different species," J. Photochem. Photobiol. B **31**(3), 101–112 (1995).
40. W. Hu, H. Li, C. Wang, S. Gou, and L. Fu, "Characterization of collagen fibers by means of texture analysis of second harmonic generation images using orientation-dependent gray level co-occurrence matrix method," J. Biomed. Opt. **17**(2), 026007 (2012).
41. K. Enarsson, E. Johnsson, C. Lindholm, A. Lundgren, Q. Pan-Hammarström, E. Strömberg, P. Bergin, E. L. Baunge, A. M. Svennerholm, and M. Quiding-Järbrink, "Differential mechanisms for T lymphocyte recruitment in normal and neoplastic human gastric mucosa," Clin. Immunol. **118**(1), 24–34 (2006).
42. W. Hu and L. Fu, "Simultaneous characterization of pancreatic stellate cells and other pancreatic components within three-dimensional tissue environment during chronic pancreatitis," J. Biomed. Opt. **18**(5), 056002 (2013).
43. A. Zakaryan, K. Karageuzyan, L. Hovsepyan, L. Karabashyan, and G. Zakaryan, "Quantitative analysis of phospholipids and gangliosides in bone marrow progenitors of lymphocytes, thymocytes and mature lymphocytes in tumor-bearing animals," Int. Immunol. **13**(9), 1141–1145 (2001).
44. D. R. Fooksman, T. A. Schwickert, G. D. Victora, M. L. Dustin, M. C. Nussenzweig, and D. Skokos, "Development and migration of plasma cells in the mouse lymph node," Immunity **33**(1), 118–127 (2010).
45. R. Orzekowsky-Schroeder, A. Klinger, S. Freidank, N. Linz, S. Eckert, G. Hüttmann, A. Gebert, and A. Vogel, "Probing the immune and healing response of murine intestinal mucosa by time-lapse 2-photon microscopy of laser-induced lesions with real-time dosimetry," Biomed. Opt. Express **5**(10), 3521–3540 (2014).
46. A. Klinger, R. Orzekowsky-Schroeder, D. von Smolinski, M. Blessenohl, A. Schueth, N. Koop, G. Huettmann, and A. Gebert, "Complex morphology and functional dynamics of vital murine intestinal mucosa revealed by autofluorescence 2-photon microscopy," Histochem. Cell Biol. **137**(3), 269–278 (2012).
47. P. Lauren, "The two histological main types of gastric carcinoma: diffuse and so-called intestinal-type carcinoma. An attempt at a histo-clinical classification," Acta Pathol. Microbiol. Scand. **64**(1), 31–49 (1965).
48. H. J. Shin and J. L. Mego, "A rat liver lysosomal membrane flavin-adenine dinucleotide phosphohydrolase: purification and characterization," Arch. Biochem. Biophys. **267**(1), 95–103 (1988).

1. Introduction

Stomach cancer is the fifth most commonly diagnosed cancer and the third leading cause of cancer death worldwide [1, 2]. 90% of the stomach cancers are gastric adenocarcinomas [2, 3]. Gastric carcinogenesis is a long-term and multistep process, which generally involves a progression from normal mucosa through chronic gastritis, atrophic gastritis, and intestinal metaplasia, to dysplasia and carcinoma [4]. Chronic gastritis caused by Helicobacter pylori infection is the primary instigator of intestinal metaplasia and subsequent adenocarcinoma formation [2]. Intestinal metaplasia would be the earliest indicator of potential malignant progression to gastric carcinoma [4–6]. Identification and treatment of these premalignant and malignant lesions of gastric mucosa at the early stage is crucial to decrease the incidence and mortality of stomach cancer.

Gastroscopy for primary detection and biopsy specimen collection, followed by the gold standard histopathological examination for final confirmation, is the routine method used in clinic for gastric disease diagnosis. However, this method is invasive and extremely time-consuming (3–5 days) [7, 8]. It is highly desirable to develop a technology for performing real-time histological diagnosis during routine endoscopy. To meet this demand, a variety of gastroscopic imaging techniques have been developed for better visualization of cellular and subcellular details with enhanced contrast and resolution. Typical examples include chromoendoscopy [9], narrow-band imaging [10], autofluorescence endoscopy [11], magnifying endoscopy [12], and different combinations of these techniques [13–15]. Compared with conventional gastroscopy, these techniques have improved the detection rate of premalignant gastric lesions and early gastric cancers. But, due to the limited resolution (> 5 μm) [12], they are still far less accurate than histopathological examination. In recent years, confocal laser endomicroscopy with subcellular resolution (down to 0.7 μm) has emerged as a noninvasive on-site imaging modality of gastric mucosa, potentially bringing a revolutionary leap toward the *in vivo* diagnosis of gastric diseases [16, 17]. This technique has been proven to be able to provide histology-like images of tissues, while avoiding the risks and costs of conventional biopsies [16]. However, exogenous fluorescence agents, such as fluorescein or

Biomedical Optics EXPRESS

acriflavine hydrochloride, have to be applied to provide sufficient contrast by highlighting the structure and physiology of nucleus, cytoplasm, or vasculature. These agents are not FDA-approved for this kind of clinical application [16]. As a more powerful imaging tool, multiphoton microscopy (MPM) based on two-photon excited fluorescence (TPEF) and second harmonic generation (SHG) has attracted lots of attention since it was developed [18, 19]. This imaging modality is not only capable of producing images with similar details of standard histology by detecting intrinsic fluorescence chromophores, but also possesses superior tissue penetration depth, reduced photobleaching and photodamage, and intrinsic three-dimensional (3D) sectioning ability [18–20]. Due to these attractive advantages over confocal laser microscopy, MPM has been widely applied in the investigation of normal and diseased gastrointestinal tissues [6, 8, 21–23].

Nonetheless, all of the above techniques are confined to qualitative morphological characterizations. Pathological change is associated with not only structural but also biochemical variations of fluorescent biomolecular complexes in cells and tissues [24]. A combined detection of biological properties on both aspects may provide more powerful diagnostic capabilities. The recently emerged spectrum- and time-resolved techniques open up new ingenious approaches for accessing quantitative biochemical information of living tissues [25]. Specifically, fluorescence spectra can be regarded as the characteristic "fingerprints" of each fluorophore and provide unique identification and separation in complex biological systems [25]; fluorescence lifetime properties provide an additional approach for fluorophore separation even when the fluorophores have overlapping spectra [24, 25]. Moreover, fluorescence lifetime is sensitive to various parameters of the biological microenvironment, such as pH, temperature, oxygen saturation, ionic concentration, enzymatic activity, etc., as well as bonds or molecular associations [24, 25]. Therefore, it can be used to characterize variations of the local molecular environment and interactions between proteins [24, 26]. More importantly, the property that fluorescence lifetime is independent of fluorophore concentration and quantum yield, enables more precise biophysical measurements of cells and tissues [24, 26]. Based on these advantages, fluorescence spectrum and lifetime detection has received considerable attention and been widely used in biophysics and medical diagnostic researches [27–30]. The further combination of MPM with these technologies empowers detailed morphological and biochemical characterization of tissues, by comprehensively detecting 3D fluorescence intensity, spectrum, and lifetime distribution with subcellular resolution [25, 29]. Despite the recognized inherent advantages, the full potential of spectrum- and time-resolved MPM has not been extensively evaluated in clinical settings.

In this study, we report for the first time (to the best of our knowledge), the systematic investigation on human gastric carcinogenesis by spectrum- and time-resolved MPM imaging of its multiple typical stages, including normal, chronic gastritis with erosion (CG-E), chronic gastritis with intestinal metaplasia (CG-IM), and intestinal-type adenocarcinoma (ITA). Since the ultimate value of the technique would be nondestructive *in vivo* "optical biopsy" by endoscope, all the imaging experiments were performed from the prospective of gastroscope. By comparatively analyzing the spectrum- and time-resolved endogenous multiphoton signals, qualitative and quantitative structural and biochemical features of gastric mucosa at typical stages of gastric carcinogenesis were derived. The results not only demonstrate the value of the technique for imaging gastric mucosa but also affirm its significant potential for discriminating different gastric disorders using only endogenous contrast. This study fills the knowledge gap of human gastric diseases under spectrum- and time-resolved MPM imaging and may shed new light on the early diagnosis of premalignant and malignant lesions of the stomach. We note that there are increasing interests in developing multiphoton endoscopes for clinical use [7, 31, 32], and these advances make it promising to miniaturize the spectrum- and time-resolved MPM for noninvasive, label-free, real-time histological and functional diagnosis of gastric diseases in the future.

Biomedical Optics EXPRESS

2. Materials and methods

2.1 Human gastric mucosa specimens

As gastric antrum is the most common site of gastric carcinoma [2], normal and diseased human gastric antrum mucosa specimens from 12 patients of Peking University Shenzhen Hospital (Shenzhen, China) were collected by gastroscopy or surgical resection for the study. These samples include 3 normal specimens beside pathological tissues, 4 specimens with CG-E, 2 specimens with CG-IM, and 3 ITA specimens. In all cases, the clinical diagnosis was confirmed by standard histopathological examination. This was performed by using half of each specimen to prepare routine hematoxylin and eosin (H&E) stained sections and then diagnosed by professional pathologists. The remaining half of the specimen was immediately imaged by MPM within 2 hours. The tissue was firstly placed in a custom-designed groove filled with phosphate buffered saline, and then covered with a microscope coverslip. The surface of the gastric mucosa was kept against the coverslip. To avoid overcrowding of the sample, the groove's height was designed to be similar to the thickness of the tissue. To get a representation of the normal and diseased human gastric mucosa, 3–5 sites from each specimen were randomly chosen and imaged. All the patients who participated in the study provided their written informed consent and the experimental procedures were performed under the supervision and approval of the Ethics Committee for Human Research, Peking University Shenzhen Hospital (Ethics Approval No. 1427611284372).

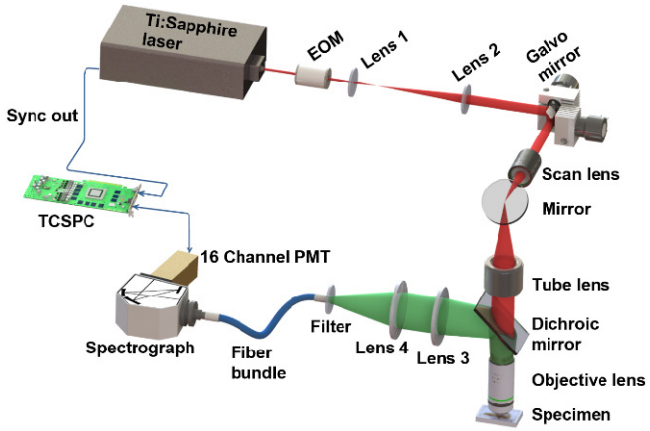

Fig. 1. Schematic diagram of the spectrum- and time-resolved MPM imaging system.

2.2 Imaging instrumentation

To obtain the spectrum- and time-resolved multiphoton signals of human gastric mucosa, a home-built MPM imaging system [28] was used. Figure 1 shows the schematic diagram of the system. Briefly, a femtosecond Ti:Sapphire laser (Chameleon Ultra, Coherent) tuned to 750 nm was utilized as the excitation source. The expanded laser beam was raster scanned by a pair of galvanometer mirrors (TSH8310, Sunny Technology) to create images of the sample with a size of 256 μm × 256 μm or 360 μm × 360 μm and a pixel dimension of 128 × 128. After the scanners, the beam passed through a scan lens, a tube lens, a dichroic mirror (FF685-Di02, Semrock), and then was focused on the specimen by a 20 × , 1.0 NA water-immersion objective (XLUMPLFLN, Olympus) to excite multiphoton signals including SHG and TPEF. The backscattered signals were collected by the same objective and split from the excitation laser by the above dichroic mirror. A 680 nm short-pass filter (FF01-680/SP-25, Semrock) was further used to remove the residual excitation light. Then, the signals were collected using a fiber bundle and conducted to a spectrograph. A linear-array photomultiplier tube (PMT, PML-16-C, Becker & Hickl GmbH) was used to record the signals output from

Biomedical Optics EXPRESS

the spectrograph into 16 consecutive spectral bands with central wavelengths ranging from 354.5 nm to 542 nm at an interval of 12.5 nm. A time-correlated single photon counting module (TCSPC, SPC-150, Becker & Hickl GmbH) was further connected to the detector for recording the fluorescence decay curve of each spectral band into 256 time channels. The instrument response function of the imaging system, measured by the reflection of the femtosecond laser light, is approximately 220 ps at full width half maximum. For 3D imaging, the objective was axially translated by an actuator at a depth of 5 μm.

2.3 Segmentation of the structural components of gastric mucosa

The gastric mucosa contains many gastric pits. Each gastric pit is surrounded by a peripheral wall formed by a layer of surface epithelium and interstitial tissue fills the space between the gastric pits (refer to section 3.1 for details) [33]. To investigate the optical characteristics of the gastric mucosa in detail, we defined three structural components: mucosal surface (MS), peripheral wall of gastric pits (PWGP), and interstitial tissue between gastric pits (ITGP). Briefly, the tissue from surface to a depth of ~15 μm was defined as MS, whereas the peripheral wall and interstitial tissue at a depth ranging from ~50 μm to ~80 μm were defined as PWGP and ITGP, respectively.

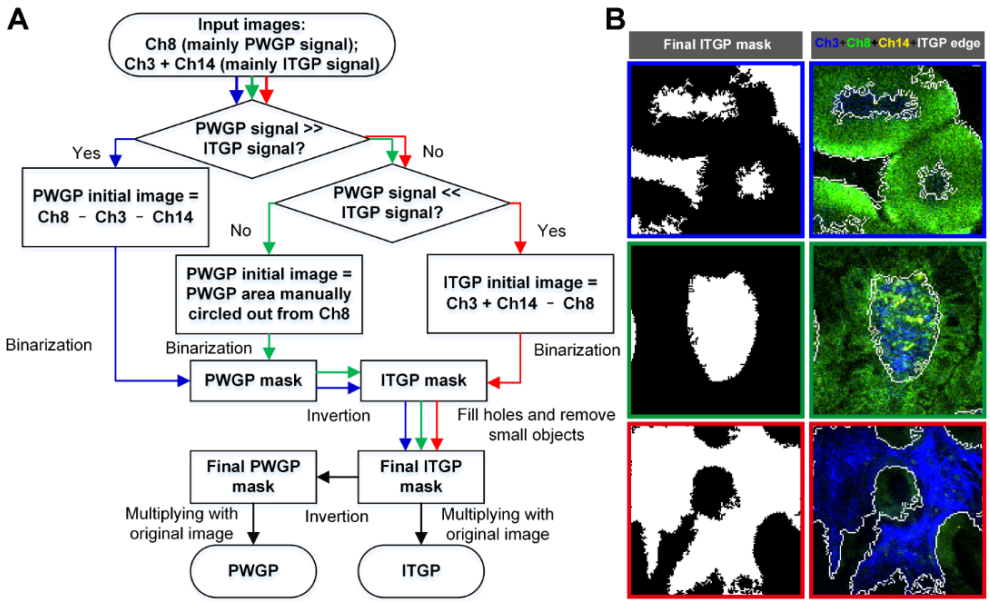

Fig. 2. Image segmentation algorithm for separating PWGP and ITGP. (A) Algorithm flow chart. (B) The final segmentation results of exemplar images (left column) and the pseudo-color merged images of raw Ch3, Ch8, and Ch14 images as well as the ITGP edges (right column). The blue, green, and red border images are processed through the blue, green, and red paths in the flowchart, respectively.

In practice, it was straightforward to identify MS from the image stacks, while an image segmentation algorithm was used to separate PWGP and ITGP (Fig. 2). Specifically, since spectral channel 8 (Ch8, 442 ± 6.25 nm) mainly contains the signal of PWGP, while signals in spectral channels 3 and 14 (Ch3, 379.5 ± 6.25 nm; Ch14, 517 ± 6.25 nm) mainly come from ITGP, we first estimated the initial image of one of the two components by image arithmetic of the three spectral channels as follows: for imaging area with strong PWGP but weak ITGP signals, the PWGP initial image was obtained as Ch8 – Ch3 – Ch14; in the opposite case, the ITGP initial image was obtained as Ch3 + Ch14 – Ch8; in other cases, we manually circled out the area of PWGP from the Ch8 image to obtain its initial image. Second, a binary mask of the initial image was created using a threshold of 0. Third, holes

Biomedical Optics EXPRESS

less than 2000 μm^2 in the resulting binary image were filled, and small objects, defined as occupying an area of less than 400 μm^2, were removed from the mask [34]. Notably, PWGP mask was inverted to become an ITGP mask before filling holes, since the filling-hole operation could fill the hole in the center of the donut-shaped PWGP and thus produce an incorrect PWGP mask. Finally, the ITGP was simply separated from PWGP by multiplying the final mask with the original image. The first step was performed by ImageJ software (National Institutes of Health) and the other steps were carried out using a custom MATLAB (MathWorks) program.

2.4 Fluorescence spectrum and lifetime measurements

To reveal the general spectral characteristics of the gastric mucosa, spectrum-coded images were created according to the following strategy. First, a specific RGB color was assigned to a given spectral channel. Second, the color-weighted intensity image of the channel was calculated by multiplying the intensity of each pixel with the RGB color. Third, the 16 color-weighted intensity images added up to a spectrum-coded image. To do structural component-resolved spectral analysis, the signals of MS, PWGP and ITGP from each spectral channel in one *z*-section were separately integrated to produce their respective spectral curves. From the spectral curve, fluorescence spectral parameters, including SHG/TPEF (the ratio of signals from the channel with maximum SHG (Ch3, 379.5 ± 6.25 nm) over those from the channel with maximum TPEF (Ch8, 442 ± 6.25 nm or spectral channel 9 (Ch9, 454.5 ± 6.25 nm))) and TPEF spectral ratio (the ratio of TPEF signals with long wavelength (Ch14, 517 ± 6.25 nm) over those with short wavelength (spectral channel 6 (Ch6, 417 ± 6.25 nm))), were calculated. The above spectral analyses were performed using custom MATLAB programs.

To compute fluorescence lifetime parameters, the fluorescence decay curve was deconvolved with the instrument response function of the imaging system and subsequently fitted with a dual exponential function model—$\alpha_1 e^{-t/\tau_1} + \alpha_2 e^{-t/\tau_2}$, where τ_1 and τ_2 are the time-decay constants while α_1 and α_2 are the amplitudes of the two decay terms, respectively [28, 30, 35]. Based on TPEF decay curves (the integration of spectral channels 5 to 16 (Ch5–Ch16, 398.25–548.25 nm)), the mean fluorescence lifetime—$\tau_{mean} = (\alpha_1\tau_1 + \alpha_2\tau_2)/(\alpha_1 + \alpha_2)$ for each pixel was calculated and then color coded to generate fluorescence lifetime images. To reveal more detailed TPEF lifetime characteristics, τ_1, τ_2, α_1/α_2, and τ_{mean} of Ch8 (442 ± 6.25 nm) signals which covers the intensity peak of TPEF, were particularly calculated for the multiple structural components—MS, PWGP and ITGP. Here, the signals within a given structural component in one *z*-section were integrated to improve the signal-to-noise ratio of a decay curve and each decay curve represents a single data point. In some cases, the sum of ITGP signals from a single *z*-section was still so weak that several successive *z*-sections had to be integrated to create a Ch8 (442 ± 6.25 nm) decay curve with a peak ≥ 1000 photons for calculation. The fluorescence lifetime-coded images were produced by SPCImage software (Becker & Hickl GmbH) and the other calculations were performed with custom MATLAB programs.

Table 1. Sample summary

	Patient	Total imaging site	Data point[a]			
			MS-Spectra/Lifetime[b]	PWGP-Spectra/Lifetime	ITGP-Spectra	ITGP-Lifetime
Normal	3	12	48	94	94	23
CG-E	4	13	52	97	97	71
CG-IM	2	10	40	70	70	48
ITA	3	13	60	94	94	60

[a]Data point: one *z*-section of each imaging site corresponds to one data point. In some cases of ITGP-Lifetime, several successive *z*-sections were integrated to create a decay curve with a peak ≥ 1000 photons for analysis.
[b]Lifetime: fluorescence lifetime analysis of signals from Ch8 (442 ± 6.25 nm).

Biomedical Optics EXPRESS

2.5 Statistical analyses

The data size of this study is summarized in Table 1. Statistical analyses were performed with GraphPad Prism software (GraphPad Software). For the comparison of three groups or more, the one-way ANOVA followed by the Tukey's multiple comparison test was used. In our statistical analyses, successive *z*-sections from one imaging site were treated as being independent even though this assumption is not valid.

2.6 Abbreviations

Abbreviations used in this study are summarized in Table 2.

Table 2. Abbreviations used in this study

MPM	Multiphoton microscopy
TPEF	Two-photon excited fluorescence
SHG	Second harmonic generation
3D	Three-dimensional
CG-E	Chronic gastritis with erosion
CG-IM	Chronic gastritis with intestinal metaplasia
ITA	Intestinal-type adenocarcinoma
H&E	Hematoxylin and eosin
EOM	Electro-optical modulator
PMT	Photomultiplier tube
TCSPC	Time-correlated single photon counting module
MS	Mucosal surface
PWGP	Peripheral wall of gastric pits
ITGP	Interstitial tissue between gastric pits
NADH	Reduced nicotinamide adenine dinucleotide
FAD	Flavin adenine dinucleotide

3. Results and discussions

3.1 Structure and intrinsic-contrast origin of gastric mucosa

The mucosa is the innermost layer of the stomach wall and where gastric diseases always originate. The mucosa contains a surface epithelium, lamina propria, and muscularis mucosae [33]. In our experiment of MPM imaging, we can access a depth range from the surface epithelium to the upper portion of the lamina propria (Fig. 3). The surface epithelium, covering the entire luminal surface and lining the gastric pits, are composed of well-polarized mucous epithelial cells of simple columnar type. The apical cytoplasm of the cell is filled with plentiful mucous secretory granules, which secrete neutral glycoprotein mucus. The mucus forms a film to protect the mucosa from the high concentration of hydrochloric acid and pepsin in the stomach. Mitochondria in the cell are scattered in the middle and lower cytoplasm, and the nucleus has an ovoid shape and is located in the basal region (Fig. 3). The lamina propria is a fine connective tissue, housing gastric glands that open into the bottom of the gastric pit. In the upper portion of the lamina propria, connective tissue, which is also called interstitial tissue, fills the spaces between gastric pits. The interstitial tissue consists of a delicate meshwork of collagen fibers with a few fibroblasts, some plasma cells, a small amount of smooth muscle fibers, and a few sparsely distributed capillaries (Fig. 3) [33].

The MPM imaging in this study was performed at an excitation wavelength of 750 nm for inducing intrinic TPEF signals that mainly originate from reduced nicotinamide adenine dinucleotide (NADH) and genereting SHG signals that primarily come from collagen [19, 36]. NADH is predominantly located within the mitochondria in the cytoplasm and shows an emission spectrum with a peak at ~445 nm (covered by Ch8 (442 ± 6.25 nm)) [30]. In particular, the ratio of free to protein-bound NADH, which reflects the balance between oxidative phosphorylation and glycolysis, has long served as an indicator of cellular metabolic state [37–39]. Collagen is distributed in the extracellular matrix and has been reported to be the major contributor to the SHG signals in the biological tissues due to its

Biomedical Optics EXPRESS

non-centrosymmetrical structure [19, 36, 40]. The SHG signal peaks at 375 nm (covered by Ch3 (379.5 ± 6.25 nm)) in our experiment.

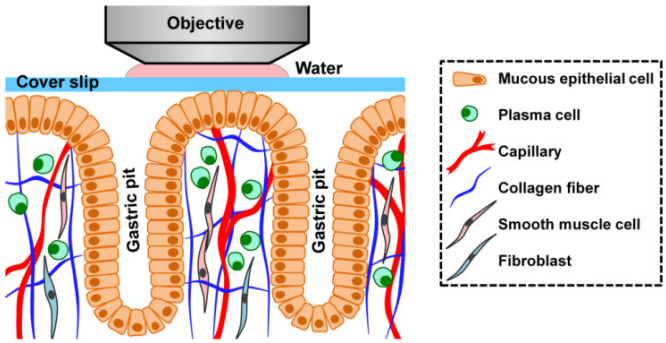

Fig. 3. Schematic diagram of the gastric mucosa with epithelium, upper portion of lamina propria, and gastric pits (longitudinal view, not true to scale).

3.2 Spectrum-coded 3D structure of gastric mucosa

In order to validate the ability of fluorescence spectra to reveal the structures of the gastric mucosa and further characterize the pathological status of the stomach, the spectrum-coded MPM images of fresh human gastric antrum mucosa of normal, CG-E, CG-IM, and ITA were created and compared with corresponding H&E stained histology images (Fig. 4). In the spectrum-coded images (the first five rows in Fig. 4), the surface epithelium delineated by the NADH TPEF signal appears as green; the collagen visualized by SHG signals appears as blue in the interstitial tissue of lamina propria; the inflammatory cells presenting in lamina propria appear as yellow, mainly consisting of plasma cells and lymphocytes, and possibly revealed by the TPEF signal of NADH as well as phospholipids. Here, the types and fluorescence origins of the inflammatory cells (pink arrows in Fig. 4) are deduced from previous studies. Some plasma cells are scattered in the lamina propria in normal tissue (Fig. 3) [33], while chronic gastritis or gastric cancer will increase the infiltration of inflammatory cells, which mainly consists of lymphocytes [41]. Lymphocytes within gastric lamina propria and pancreas with chronic inflammation have been identified by their oval shape and higher fluorescence intensity at the wavelength range of 510–550 nm [22, 23, 42], consistent with the features of the yellow inflammatory cells that we observed (pink arrows in Fig. 4). The fluorescence was possibly originated from phospholipids, a significant component of lymphocytes [23, 43]. Since plasma cells are differentiated from B lymphocytes [44], they show similar morphology and endogenous fluorescence as lymphocytes.

Based on the identified sub-structures above, the spectrum-coded MPM images of normal and diseased gastric antrum mucosa (the first five rows in Fig. 4) not only show 3D structures consistent with corresponding H&E stained histology images (the last row in Fig. 4), but also provide a more specific indication of collagen fibers via their SHG signals. In normal tissues, the superficial sections show a regular cobblestone appearance of the epithelium (0-μm depth in Fig. 4(A)). Individual mucous epithelial cell can be identified in the epithelium surface (yellow arrows in Fig. 4(A)). Their nuclei can also be delineated in the basal part of epithelium (magenta arrows in Fig. 4(A)). Narrow interstitial tissue with little collagen and plasma cells is observed beneath the surface epithelium and between gastric pits (orange arrowheads in Fig. 4(A)). The gastric pits have a branched opening in superficial layers, while appear as uniformly distributed ovals with even size in their bottom layers (white arrowheads in Fig. 4(A)).

Biomedical Optics EXPRESS

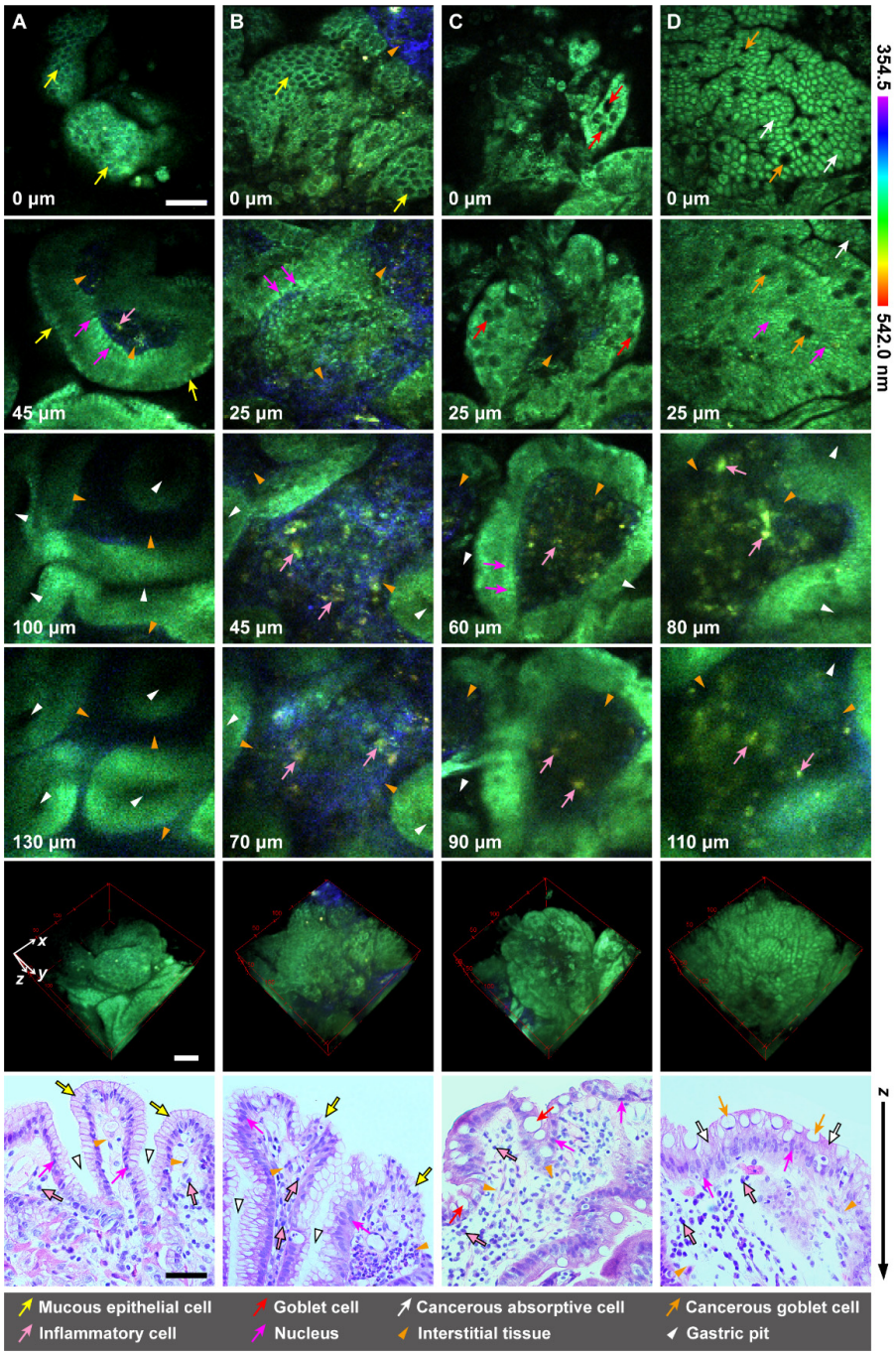

Fig. 4. Spectrum-coded 3D structures and corresponding histology of the normal and diseased human gastric antrum mucosa: (A) normal; (B) chronic gastritis with erosion; (C) chronic gastritis with intestinal metaplasia; (D) intestinal-type adenocarcinoma. The spectrum-coded images with different depths (transverse view) and corresponding 3D images are shown in the first four rows and the fifth row, respectively. The depth is labeled in the bottom left corner of each panel. The H&E stained histology images (longitudinal view) are displayed in the last row. Scale bars are 50 μm.

Biomedical Optics EXPRESS

For the diseased specimens, we find something in common, when compared with the normal tissue. First, the interstitial tissue is obviously broadened (orange arrowheads in Fig. 4(B)–4(D)) and filled with remarkably increased inflammatory cells (pink arrows in Fig. 4(B)–4(D)). Second, the gastric pits tend to become more and more blurry as disease progresses (white arrowheads in Fig. 4(B)-4(D)).

In spite of these common features, the specimens with different diseases show some distinctive structural characteristics. For the specimen with CG-E, irregularly distributed mucous epithelial cells with uneven size are observed in the surface epithelium (yellow arrows in 0-μm depth and histology image in Fig. 4(B)). Notably, some mucous epithelial cells shed from the epithelium, resulting in the leaking out of partial interstitial tissue to the mucosa surface (orange arrowhead in the top right corner of the 0-μm depth image and orange arrowhead in the bottom right corner of the histology image in Fig. 4(B)). Besides, the collagen within the interstitial tissue obviously increases (orange arrowheads in Fig. 4(B)).

Intestinal metaplasia is the transformation of gastric epithelium into a type of epithelium resembling that found in the intestine [6]. In terms of CG-IM, irregularly distributed cells, which might be intestinal absorptive cells, are found in the epithelium (0-μm depth and histology image in Fig. 4(C)). Meanwhile, goblet cells (red arrows in Fig. 4(C)) are observed scattering among the absorptive cells, which is a histopathological criterion of intestinal metaplasia [4, 6]. Goblet cells have a slender base that contains a nucleus and an expanding apex with mucous secretory granules [33]. These granules appear dark in the MPM images due to the absence of fluorescence signal (red arrows in Fig. 4(C)) [45], facilitating the identification of the goblet cells. In addition, little collagen is found in the interstitial tissue of CG-IM (orange arrowheads in Fig. 4(C)).

As for ITA specimens (Fig. 4(D)), the epithelium show almost identical histological pattern to that found in the intestine [33, 46], consisting of regularly distributed cancer cells in the morphology of absorptive cells with scattered cancerous goblet cells (0-μm depth, 25-μm depth, and histology image in Fig. 4(D)). This is consistent with ITA's histology described by the classical Laurén classification for gastric carcinomas [47]. Unlike gastric mucous epithelial cells (yellow arrows in Fig. 4(A) and 4(B)), the apical cytoplasm of intestinal absorptive cells (white arrows in Fig. 4(D)) exhibits a strong fluorescence signal, which originates from the mitochondrial NADH, while cellular interfaces appear as relatively darker lines between the absorptive cells in superficial sections (0-μm depth in Fig. 4(D)) [45]. Similar to CG-IM, little collagen is observed in the interstitial tissue of ITA (orange arrowheads in Fig. 4(D)).

Overall, the above results demonstrate that, the sub-structures of gastric mucosa including surface epithelium, fibrillar collagen, and inflammatory cells can be clearly identified in the spectrum-coded MPM images. The interstitial tissue of lamina propria is distinctively delineated by the collagen and inflammatory cells. Based on the features of these sub-structures in 3D space, normal status, different premalignant lesions, and carcinoma of the stomach can be distinguished.

3.3 Quantitative spectral characterization of the multiple components of gastric mucosa

To investigate the fluorescence spectral characteristics of the gastric mucosa in detail, we defined three structural components: MS, PWGP, and ITGP (refer to section 2.3). Based on the definition, multiple spectral parameters, including SHG/TPEF, the spectra of TPEF, and TPEF spectral ratio (refer to section 2.4), were further involved to quantitatively analyze the multiple structural components of normal and diseased gastric mucosa.

In general, how the spectral characteristics change from MS to ITGP show similar tendency for normal, benign, and malignant gastric mucosa (Fig. 5). In terms of SHG/TPEF, MS and PWGP show close proximity of values due to the same composition—epithelium; whereas ITGP shows obviously increased values due to more collagen fibers in the lamina

Biomedical Optics EXPRESS

propria (Fig. 5(A)). The TPEF spectra of MS and PWGP are almost the same and consistent with the typical NADH spectrum [30]; whereas that of ITGP shows a red shift and higher intensity at about 500–550 nm (Fig. 5(B)). The difference is probably attributed to the fluorescence from inflammatory cells. These cells are found to have a vice fluorescence peak at ~517 nm (black circles in Fig. 5(B)), consistent with the feature of lymphocytes reported in previous studies [22, 23, 42]. Notably, the difference becomes more and more obvious from normal, to benign, to malignant specimens (Fig. 5(B)), indicating an gradual increase in inflammatory-cell invasion. Thus, this difference can be considered as a potential indicator for the discrimination of normal gastric tissue, benign gastric disease, and malignant gastric disease. Furthermore, the spectral shift and intensity variation were quantified by TPEF spectral ratio, as shown in Fig. 5(C).

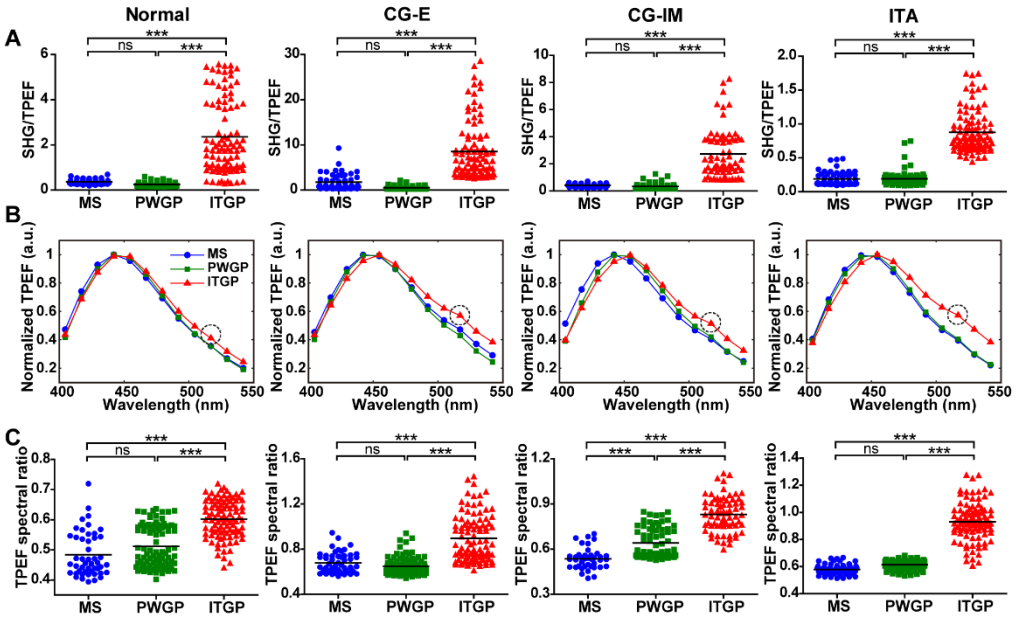

Fig. 5. Spectral characteristics of the multiple components of the normal and diseased human gastric antrum mucosa: comparison of different structural components including mucosal surface (MS), peripheral wall of gastric pits (PWGP), and interstitial tissue between gastric pits (ITGP). (A) The ratio of SHG signal to TPEF. (B) The spectra of TPEF. The error bars denote the SEM. The black circle marks out the vice fluorescence peak. (C) The ratio of TPEF with long wavelength (517 ± 6.25 nm) to that with short wavelength (417 ± 6.25 nm). The black solid lines in (A) and (C) indicate the mean values. ns: no significant difference; ***: $P < 0.001$, one-way ANOVA and Tukey's multiple comparison test.

Note that for the specimens with CG-E, the presence of collagen fibers and inflammatory cells in MS, caused by the local shedding of mucous epithelial cells, doesn't result in substantial discrepancy in the spectral characteristics of MS from those of PWGP (CG-E in Fig. 5). Another exception is CG-IM. As shown in CG-IM in Fig. 3(B) and 3(C), there is an obvious red shift of TPEF spectra and significant increase in TPEF spectral ratio for PWGP relative to MS. CG-IM is featured with intestinal metaplasia. Since lymphocytes are found ~17 μm beneath the surface of intestinal epithelium [45] while MS only contains mucosa tissues at a depth of 0–15 μm, more lymphocytic signals can be captured in PWGP than MS by 3D imaging, and thus leading to the above spectral variation.

Based on the above analysis, we directly compared the spectral characteristics of the same structural component of gastric mucosa for normal and diseased specimens (Fig. 6). In terms of the MS, CG-E is featured with the presence of collagen fibers and inflammatory cells due to the local shedding of mucous epithelial cells. As a result, CG-E shows the highest

Biomedical Optics EXPRESS

SHG/TPEF value and TPEF spectral ratio compared with other specimens (MS in Fig. 6). Moreover, the TPEF spectra of CG-IM and ITA show a slight red shift relative to the normal tissue and the TPEF spectral ratio, which quantifies the red shift, is found to gradually increase from normal, to CG-IM, to ITA (MS in Fig. 6(B) and 6(C)). The statistically significiant red shifts suggest a difference in the composition of endogenous chromophores of mucous epithelial cells, absorptive cells, and cancerous absorptive cells.

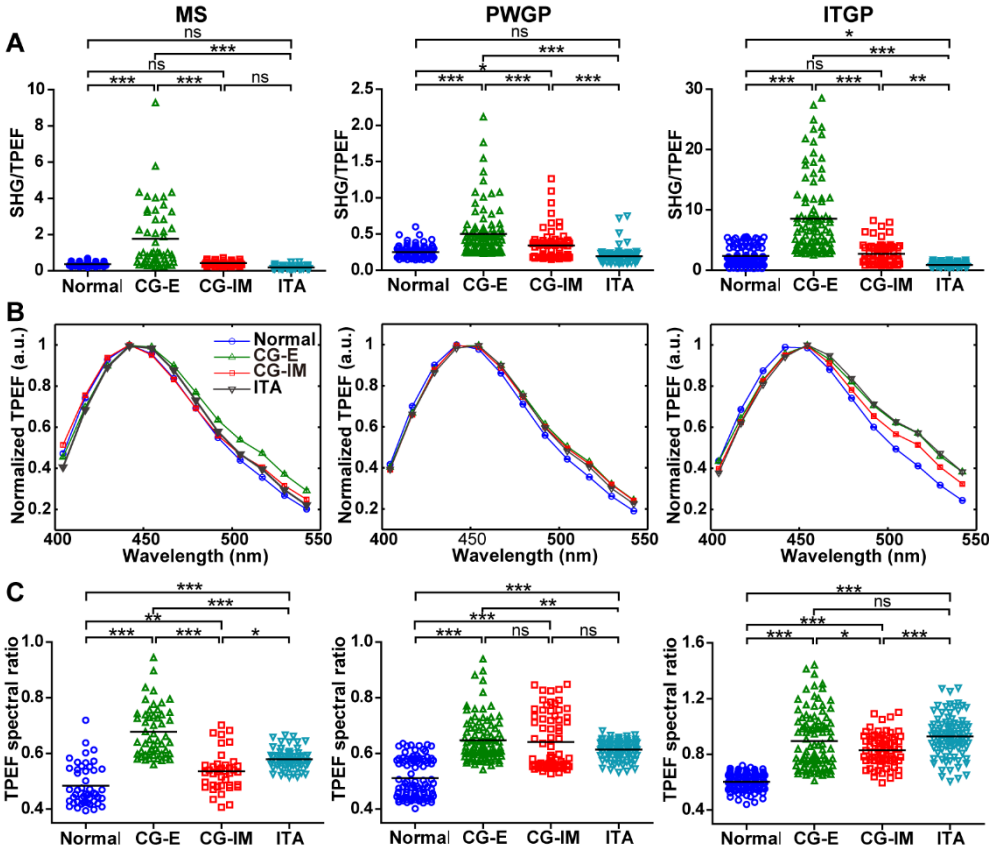

Fig. 6. Spectral characteristics of the multiple components of the normal and diseased human gastric antrum mucosa: comparison of normal tissue and diseased tissues of chronic gastritis with erosion (CG-E), chronic gastritis with intestinal metaplasia (CG-IM), and intestinal-type adenocarcinoma (ITA). (A) The ratio of SHG signal to TPEF. (B) The spectra of TPEF. The error bars denote the SEM. (C) The ratio of TPEF with long wavelength (517 ± 6.25 nm) to that with short wavelength (417 ± 6.25 nm). The black solid lines in (A) and (C) indicate the mean values. ns: no significant difference; *: 0.01 <P < 0.05; **: 0.001 <P < 0.01; ***: P < 0.001, one-way ANOVA and Tukey's multiple comparison test.

For the PWGP, the SHG/TPEF value mainly characterizes the signal ratio of extracellular matrix over cytoplasm of epithelial cells. Since there are few collagen fibers in PWGP, the SHG/TPEF values for different specimens are all very low with mean values ranging from 0.19 to 0.50 (PWGP in Fig. 6(A)). As has been found in MS, a red shift in TPEF spectra and an obvious increase in TPEF spectral ratio are also observed between normal and diseased PWGP (PWGP in Fig. 6(B) and 6(C)). For CG-E, the TPEF spectral peak has a tendency to shift from channel 442 ± 6.25 nm to 455 ± 6.25 nm compared with the normal tissue. The TPEF signal in PWGP is dominantly from NADH which can be categorized into free and protein-bound groups. The free NADH and protein-bound NADH are known to have spectral peaks at ~452 nm and ~439 nm, respectively [30]. Therefore, the red shift might come from

Biomedical Optics EXPRESS

the change of partial NADH from protein-bound state to free ones, indicating an enhancement of mucous epithelial cells' anaerobic metabolism capability during the occurrence and development of gastritis. For CG-IM and ITA, the red shifts of the TPEF spectra relative to the normal tissue may be caused by the different endogenous chromophores of absorptive cells, cancerous absorptive cells, and mucous epithelial cells, as has been found in MS. But, contrary to MS (MS in Fig. 6(C)), no significient differece of PWGP spectral ratio is observed between CG-IM and ITA (PWGP in Fig. 6(C)). This might be a result of the extra red shift of PWGP specrum relative to MS spectrum which is induced by lymphocytes presenting in the PWGP in CG-IM specimens.

As for the ITGP, the density of collagen fibers and the amount of infiltrating inflammatory cells within the connective tissue are directly reflected in the SHG/TPEF values and the TPEF spectra, respectively. The normal tissue and CG-IM show similar SHG/TPEF values, while CG-E and ITA have remarkably higher and lower values, respectively (ITGP in Fig. 6(A)), suggesting that the benign disease and malignant disease might cause opposite alteration in the colagen density of connective tissues of gastric mocusa. TPEF spectra of diseased specimens show a considerably red shift and higher intensity at about 500–550 nm, when comparing with those of the normal specimen (ITGP in Fig. 6(B)). Meanwhile, the TPEF spectral ratios show consistent tendency (ITGP in Fig. 6(C)), indicating an infiltration of inflammatory cells as diseases occur and progress.

Moreover, we find that the difference of TPEF spectral parameter between the ITGP and PWGP can provide greater statistically significant difference among different pathological status of the stomach than directly comparing a single structural component. As shown in Fig. 7, the TPEF spectral difference at 404.5–454.5 nm gradually decreases, meanwhile the rest spectral band (454.5–542 nm) and the difference of TPEF spectral ratio gradually increase, from normal, to benign, to malignant specimens.

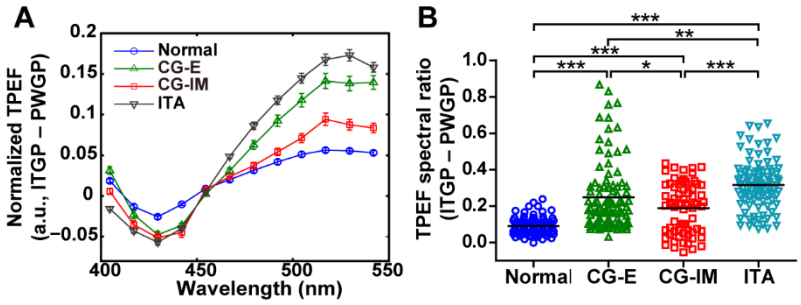

Fig. 7. The differences of TPEF spectral parameters between interstitial tissue between gastric pits (ITGP) and peripheral wall of gastric pits (PWGP). (A) The TPEF spectral difference. The error bars denote the SEM. (B) The difference of TPEF spectral ratio. The TPEF spectral ratio was computed by dividing TPEF with long wavelength (517 ± 6.25 nm) by that with short wavelength (417 ± 6.25 nm)). The black solid lines indicate the mean values. *: $0.01 < P < 0.05$; **: $0.001 < P < 0.01$; ***: $P < 0.001$, one-way ANOVA and Tukey's multiple comparison test.

In summary, these results suggest that the spectral characteristics correlate well to the tissue biochemical components. As a result, the sub-structures of gastric mucosa, such as epithelium and interstitial tissue of lamina propria, can be clearly discriminated. Furthermore, a single spectral parameter of a specific structural component (such as TPEF spectral ratio of MS) or an integration of spectral parameters of different structural components (such as the TPEF spectral difference and the difference of TPEF spectral ratio between the ITGP and PWGP) can provide statistically significant differences for identifying the normal, benign, and malignant gastric specimens tested in this study.

Biomedical Optics EXPRESS

3.4 Fluorescence lifetime-coded 3D structure of gastric mucosa

In order to evaluate the ability of fluorescence lifetime to distinguish the multiple structual components of gastric mucosa and further reveal the pathological status of the stomach, the fluorescence lifetime-coded 3D images of the normal and diseased gastric mucosa were reconstructed based on TPEF signals accroding to section 2.4. As the excited TPEF mainly originates from NADH, the fluorescence lifetime-coded 3D images principally reflect the states of mitochondrial NADH and thus the metabolic activity [37] of different cells. However, other endogenous chromophores, such as flavin adenine dinucleotide (FAD) within the lysosomal membranes [48] and phospholipids from inflammatory cells, may also be excited at the same excitation wavelength (750 nm) and responsible for the fluorescence lifetime.

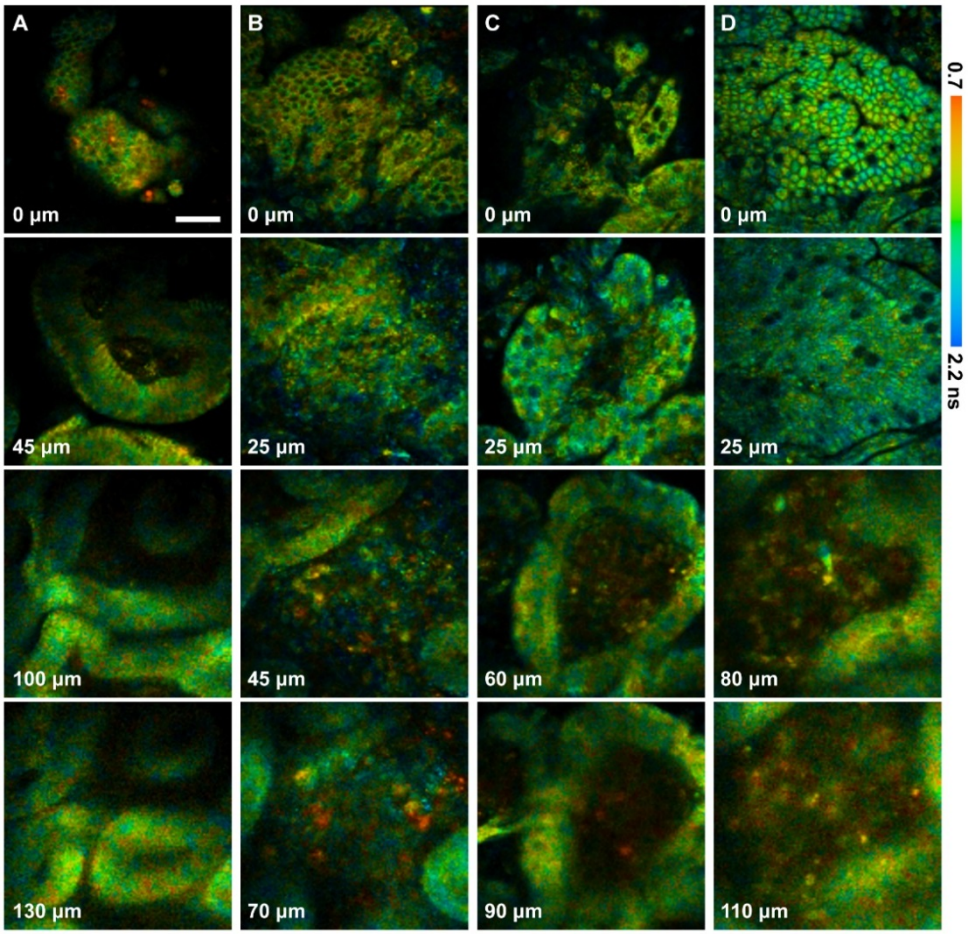

Fig. 8. Fluorescence lifetime-coded 3D structures of the normal and diseased human gastric antrum mucosa: (A) normal; (B) chronic gastritis with erosion; (C) chronic gastritis with intestinal metaplasia; (D) intestinal-type adenocarcinoma. The depth is labeled in the bottom left corner of each panel. The scale bar is 50 μm.

As shown in Fig. 8, the epithelium generaly exhibits a fluorescence lifetime ranging from yellow to green (about 0.8–1.6 ns), which are attributed to the mitochondrial NADH and a small amount of lysosomal FAD [46]. The fluorescence lifetime of MS becomes longer from normal to cancer (0-μm depth in Fig. 8), suggesting a metabolic variation of the epithlium during gastric carcinogenesis. Unlike epithelial cells, some inflammatory cells within the

Biomedical Optics EXPRESS

interstitial tissue appear as orange (last two rows in Fig. 8(B)–8(D)), indicating a shorter fluorescence lifetime. This shorter lifetime may be primarily attributed to the increased ratio of free to bound NADH relative to epithelial cells and partly attributed to phospholipids. Overall, the fluorecence lifetime-coded images reveal subcellular-resolved metabolic differences of the multiple specimens and the various cell types that is imperceptible in the spectrum-coded 3D structures. Thus, fluorescence lifetime might be capable of providing complementary information to the spectral characteristics for the differentiation of normal and diseased gastric samples.

3.5 Quantitative NADH fluorescence lifetime of the multiple components of gastric mucosa

To reveal more specific TPEF lifetime characteristics, NADH signals were unmixed by focusing only on the fluorescence collected by Ch8 (442 ± 6.25 nm, covering the peak of NADH emission spectrum at ~445 nm [30]). The corresponding lifetime parameters, including τ_1, τ_2, α_1/α_2, and τ_{mean}, were particularly calculated (refer to section 2.4). Here, τ_1 and τ_2 mainly reflect the fluorescence lifetimes of free and protein-bound NADH, respectively, while α_1/α_2 and τ_{mean} probably indicate the contribution ratio and average fluorescence lifetime of free and protein-bound NADH [35]. According to previous report, α_1/α_2 could be used to reveal the balance between oxidative phosphorylation and glycolysis, which are the primary ways for aerobic and anaerobic metabolisms, respectively [37]. Therefore, in this study, the fluorescence lifetime parameters were investigated in detail to distinguish different structural components as well as various pathological status of gastric mucosa.

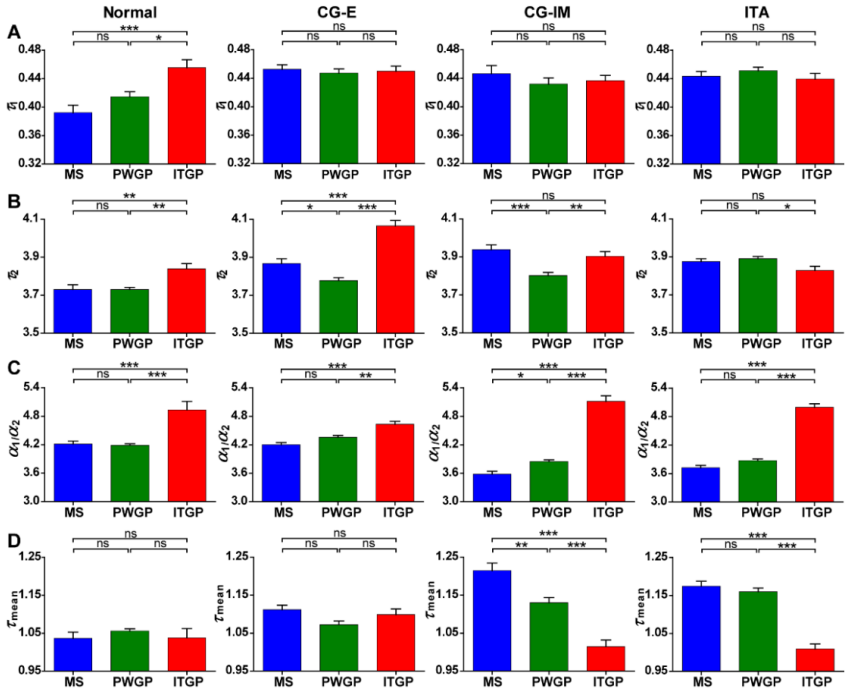

Fig. 9. NADH fluorescence lifetime characteristics of the multiple components of the normal and diseased human gastric antrum mucosa: comparison of different structural components including mucosal surface (MS), peripheral wall of gastric pits (PWGP), and interstitial tissue between gastric pits (ITGP). (A) The fluorescence lifetime of free NADH: τ_1. (B) The fluorescence lifetime of protein-bound NADH: τ_2. (C) The ratio of the amplitude coefficient of free NADH to that of protein-bound NADH: α_1/α_2. (D) The mean fluorescence lifetime: τ_{mean}. The error bars denote the SEM. ns: no significant difference; *: $0.01 < P < 0.05$; **: $0.001 < P < 0.01$; ***: $P < 0.001$, one-way ANOVA and Tukey's multiple comparison test.

Biomedical Optics EXPRESS

On average, τ_1 and τ_2 are 0.44 ns and 3.85 ns, respectively, approximating the fluorescence lifetimes of free and protein-bound NADH described in previous studies [37]. As for each structural component, we find that, ITGP has a remarkable longer τ_1 than MS and PWGP in normal specimen. However, for diseased gastric mucosa, there is no significant difference among τ_1 of the multiple structure components (Fig. 9(A)). In terms of τ_2, no uniform characteristic can be derived from different specimens (Fig. 9(B)). ITGP was found to have a higher α_1/α_2 than MS and PWGP (Fig. 9(C)), suggesting that inflammatory cells execute a lower aerobic metabolism and higher anaerobic metabolism than epithelial cells. As for τ_{mean}, the multiple structure components show similar values in normal and CG-E specimens, while ITGP has a considerable shorter τ_{mean} than MS and PWGP in CG-IM and ITA specimens (Fig. 9(D)). Particularly for CG-IM, the presence of lymphocytes in the basal part of epithelium results in a higher α_1/α_2 and shorter τ_{mean} in PWGP than MS.

Furthermore, we directly compared the fluorescence lifetime characteristics of the same structural component of normal and diseased specimens. For τ_1 and τ_2 of the MS, there is no clear distinction among the multiple diseased specimens, while the normal specimen is found to have considerable lower values than all of them (MS in Fig. 10(A) and 10(B)). The α_1/α_2 values of the MS can classify the four specimens into two groups. The first group with a relatively higher value consists of Normal and CG-E, while the other one with a relatively lower value includes CG-IM and ITA (MS in Fig. 10(C)). This indicates that, gastric mucous epithelial cells may execute a lower aerobic metabolism and higher anaerobic metabolism than intestinal absorptive cells. Meanwhile, the result demonstrates that, the presence of lymphocytes in CG-E MS, due to the partial shedding of epithelium, has no substantial influence on the overall metabolic activity of MS. Notably, τ_{mean} of the MS gradually increases as the disease progresses from normal, to CG-E, to CG-IM, while from CG-IM to ITA, the MS τ_{mean} doesn't significantly change (MS in Fig. 10(D)).

As for the PWGP, τ_1 of the normal specimen is lower than that of CG-E and ITA, while τ_2 increases from normal, to benign, to malignant specimens (PWGP in Fig. 10(A) and 10(B)). CG-E shows a significantly higher α_1/α_2 value than normal tissue (PWGP in Fig. 10(C)), indicating that the concentration ratio of free NADH over protein-bound NADH increases and the anaerobic metabolism capability of mucous epithelial cells enhances during the occurrence and development of gastritis. This variation echoes the red shift of CG-E TPEF spectra relative to the normal tissue, as shown in Fig. 6(B) and 6(C). In addition, PWGP may contain much more NADH than MS since the mitochondria in mucous epithelial cells are scattered in the middle and lower cytoplasm. Thus, the variation of the metabolic activity of mucous epithelial cells is clearly reflected on α_1/α_2 of PWGP rather than MS. CG-IM and ITA show remarkably lower α_1/α_2 values than normal and CG-E (PWGP in Fig. 10(C)), which is associated with the distinct metabolic activities of intestinal absorptive cells and gastric mucous epithelial cells. The significant earlier increase and later decrease trend of α_1/α_2 from normal, to CG-E, to CG-IM and ITA suggests that, the NADH stated metabolic activity can sensitively reflect the progression of gastric diseases. The increased τ_{mean} from normal and CG-E to CG-IM and ITA (PWGP in Fig. 10(D)) suggests that, it can be used to divide the pathologic process into two stages: before and after intestinal metaplasia.

In terms of the ITGP, τ_1 of different specimens doesn't show clear discrepancy, while τ_2 is found to be longer for CG-E than other specimens (ITGP in Fig. 10(A) and 10(B)). In addition, significant lower α_1/α_2 and longer τ_{mean} of CG-E than specimens with intestinal metaplasia (CG-IM and ITA) are observed, whereas the normal tissue shows values in between (ITGP in Fig. 10(C) and 10(D)). This result suggests two points. First, inflammatory cells within tissues of intestinal metaplasia execute a dcreased aerobic metabolism and increased anaerobic metabolism, comparing compared with those within the erosion tissue. Second, erosion and intestinal metaplasia would lead to opposite variation of inflammatory cells' metabolic activity relative to the normal tissue.

Biomedical Optics EXPRESS

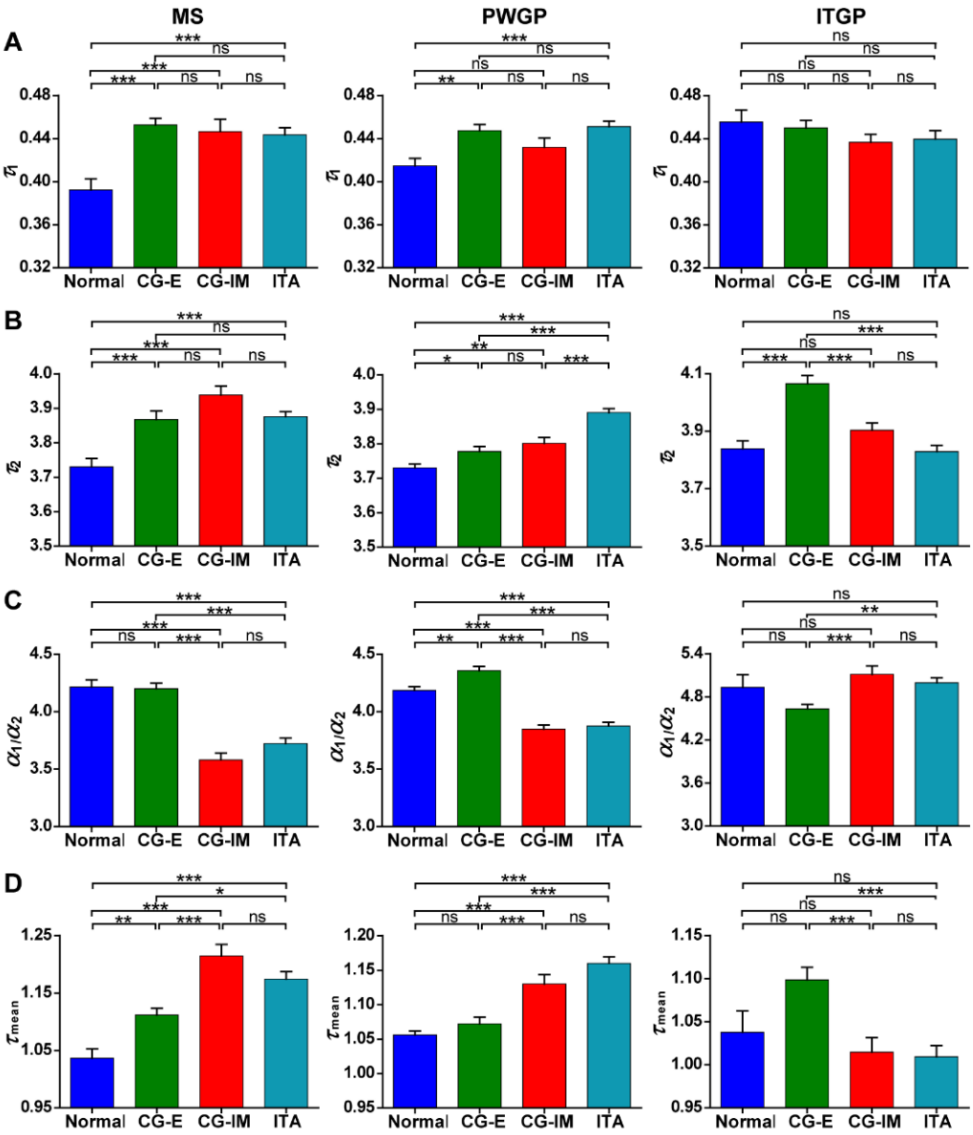

Fig. 10. NADH fluorescence lifetime characteristics of the multiple components of the normal and diseased human gastric antrum mucosa: comparison of normal tissue and diseased tissues of chronic gastritis with erosion (CG-E), chronic gastritis with intestinal metaplasia (CG-IM), and intestinal-type adenocarcinoma (ITA). (A) The fluorescence lifetime of free NADH: τ_1. (B) The fluorescence lifetime of protein-bound NADH: τ_2. (C) The ratio of the amplitude coefficient of free NADH to that of protein-bound NADH: α_1/α_2. (D) The mean fluorescence lifetime: τ_{mean}. The error bars denote the SEM. ns: no significant difference; *: $0.01 < P < 0.05$; **: $0.001 < P < 0.01$; ***: $P < 0.001$, one-way ANOVA and Tukey's multiple comparison test.

In summary, the fluorescence lifetime characteristics of NADH, mainly reflecting the cellular metabolic status, appear as useful supplements to the spectral information for the comprehensive characterization of the gastric mucosa. First, fluorescence lifetime parameters can be used to discriminate sub-structures of gastric mucosa. For instance, α_1/α_2 can differentiate epithelium and interstitial tissue of lamina propria. Second, some fluorescence lifetime parameters of specific structural components can provide statistically significant differences for identifying normal and diseased gastric samples. For example, τ_1 and τ_2 of MS can differentiate normal and disease, α_1/α_2 of MS and τ_{mean} of PWGP can determine whether

Biomedical Optics EXPRESS

the intestinal metaplasia occur, τ_2 of PWGP can differentiate normal, premalignant lesions, and carcinoma, τ_{mean} of MS and α_1/α_2 of PWGP can identify normal and different premalignant lesions. Overall, a combination of several parameters, such as τ_{mean} of MS combining with τ_2 and α_1/α_2 of PWGP, enables complete differentiation of normal, different premalignant lesions, as well as carcinoma, and thus is promising to serve as quantitative indicater for gastric disorders.

4. Conclusion

We demonstrate a multidimensional multiphoton imaging technique to comprehensively characterize the 3D structures of gastric mucosa at the typical stages of human gastric carcinogenesis, including normal, CG-E, CG-IM, and ITA. Through the measurments and analysis of intrinsic fluorescence spectral and lifetime characteristics of the tissue, we can potentially access the tissue biochemical components and cellular metabolic status at different stages of diseases. By extracting multiple spectral and lifetime parameters, the sub-structures of gastric mucosa, such as surface epithelium, interstitial tissue of lamina propria, and gastric pit, can be clearly identified. Furthermore, the spectrum- and time-resolved multiphoton signals of gastric mucosa originating from endogenous optical biomarkers can be used to generate qualitative and quantitative indicators which have the potential to discriminate the multiple stages of gastric carcinogenesis. With the development of multiphoton endoscopes and related technologies, this intravital imaging technique shows significant potential for noninvasive, label-free, real-time histological and functional diagnosis of premalignant and malignant gastric disorders. It should be noted that the sample size in this study is limited (3 normal, 4 CG-E, 2 CG-IM, and 3 ITA specimens) and successive *z*-sections from one imaging site were treated as independent data in our statistical analyses. Further studies based on more samples will be required to assess the clinical utility.

Funding

National Key Research and Development Program of China (2017YFC0110200); Program 973 (2015CB755502); National Natural Science Foundation of China (NSFC) (81471702, 81701744); China Postdoctoral Science Foundation funded project (2017M612763); Natural Science Foundation of Guangdong Province (2014A030312006, 2017A030310308); Science and Technology Planning Project of Guangdong Province (2016A020213004, 2014B050505013); Shenzhen Science and Technology Program (JCYJ20150403091443326, JCYJ20150401145529037, JCYJ20150521144321005); SIAT Innovation Program for Excellent Young Researchers (2016020).

Acknowledgments

We thank Dr. Yicong Wu for useful discussion and critical English language revision.

Disclosures

The authors declare that there are no conflicts of interest related to this article.